Journal of Alloys and Compounds, 194 (1993) 221–227
JALCOM 7209

Amorphous alloys formed by solid state reaction*

B. M. Clemens and T. C. Hufnagel
Department of Materials Science and Engineering, Stanford University, Stanford, CA 94305-2205 (USA)

(Received November 26, 1991, in final form March 26, 1992)

Abstract

Many binary systems exhibit an amorphization reaction in the solid state. Closely related to this phenomenon is the formation of disordered interfaces in metal multilayers during vapor deposition. We have observed an amorphization reaction in the Gd/Co system *in situ* during sputter deposition by using grazing incidence X-ray scattering. We relate this observation to disordered interface development in other systems, and present a simple model for bulk diffusion limited growth of the disordered layer during deposition. From the large chemical interdiffusivity calculated from this model, we conclude that other effects, perhaps surface diffusion of Co to Gd grain boundaries, are responsible for the rapid amorphization of Gd by Co.

1. Introduction

In recent years thin film multilayer structures have become increasingly important in technological applications. For instance, the active layer in a modern magnetic hard disk is a cobalt alloy thin film grown on either a chromium or amorphous nickel–phosphorus thin film, and capped with a thin carbon coating. Metal–metalloid multilayers are used for X-ray optics, Co/Pt multilayers show promise as advanced magneto-optic materials, and Fe/Cr multilayers exhibit giant magnetoresistance effects, expected to be useful for thin film magnetic recording heads.

The dimensions of technological devices are becoming progressively smaller. As the individual layers in a multilayer become thinner, interfaces comprise an increasingly larger fraction of the volume of the material. As a result, interface properties can dominate the magnetic, electronic, mechanical, and structural properties of a thin film multilayer. Fundamental studies of interface structure and properties are therefore of significant practical interest.

Schwarz and Johnson demonstrated the first solid-state amorphization reaction (SSAR) in 1983 [1]. Since that time, amorphization reactions have been demonstrated in many binary alloy systems, including transition metal/transition metal, transition metal/rare earth metal, and transition metal/metalloid pairs [2, 3]. One common process is to deposit alternating layers of crystalline elemental components on a suitable substrate. Upon annealing, the thin film transforms to an amorphous alloy via a solid-state reaction. The reaction is driven by a large negative heat of mixing between the components, which results in the amorphous alloy having a lower free energy than a two phase mixture of pure crystalline elemental phases. The formation of intermetallic phases of lower free energy than the amorphous phase is inhibited by unfavorable kinetics. Although the reaction proceeds by a diffusion limited layer growth process, grain boundary diffusion can play an important role [4, 5].

The key kinetic limitation in the solid-state amorphization reaction is the relative diffusivities of the two elements in each other and in the amorphous phase. In virtually all systems that show solid-state amorphization, one species diffuses significantly faster than the other in the amorphous phase. This mobility provides the intermixing necessary for amorphous phase growth. At the same time, crystalline intermetallic phases do not form, because nucleation of such a phase requires collective mobility in both species [3]. It is worthwhile to note that fast diffusion has been correlated with a large size difference between the components [6]. This leads to a convenient classification scheme for the propensity of different alloy systems to exhibit SSAR, based on their heat of mixing and size difference [2]. Based on such a scheme one can predict that the various Co/rare earth pairs (for example) will form amorphous alloys by solid-state reaction. Indeed, such reactions have been observed in several transition metal/rare earth systems [7–10], and Co/Gd multilayers are observed to be amorphous for a wide range of bilayer periods [11].

*Paper presented at the Symposium on Solid State Amorphizing Transformations, TMS Fall Meeting, Cincinnati, OH, October 21–24, 1991.

0925-8388/93/$6.00

2. Interfaces in metal/metal multilayer systems

2.1. Structural analysis of interfaces

A variety of analysis techniques have been employed to study the structure of interfaces in multilayers. One of the most common and most powerful is X-ray diffraction, employing the superlattice diffraction peaks characteristic of multilayers. The use of X-ray diffraction to study interfaces can be divided into two categories based on the angular range examined. Low angle ($\leqslant 15°$ 2θ) superlattice peaks are observed in the Bragg–Brentano diffraction pattern as a result of the composition modulation in the sample in a direction parallel to the sample normal. The spacing of these peaks correspond to the characteristic modulation length (the bilayer period) in the sample. The intensity of the low-angle peaks is directly related to the amplitude of the composition modulation. Therefore, information about the shape of the modulation (*e.g.* homogeneous, sinusoidal or abrupt) and the chemical interdiffusion coefficient can be obtained from these peaks. Because the low-angle superlattice peaks result from the structure of the sample on a scale of $\geqslant 25$ Å, they are relatively insensitive to the details of the interface and atomic level structure, which occur on a smaller scale.

Superlattice lines in the high-angle region, in contrast, are extremely sensitive to the nature of the interfaces between the constituents of the multilayer [12]. If the interfaces are highly ordered (*i.e.* there is a definite crystallographic registry between the constituents at the interfaces), then instead of diffraction peaks corresponding to the d-spacings of the separate components of the multilayer appearing, a single Bragg peak corresponding to the average d-spacing in the material will be present. This peak is surrounded by satellite peaks, the spacing of which are dependent on the bilayer period of the sample. At the opposite extreme, if the interfaces in the multilayer are completely disordered (so that there is no registry across the interfaces), one observes the Bragg peaks associated with each component and no superlattice peaks appear. A whole range of structures (and corresponding diffraction patterns) exists between these two extremes. It is therefore possible to deduce detailed information about the structure of the interfaces by developing an appropriate model for the diffraction pattern and fitting the results of the model to the observed pattern.

2.2. Relation between SSA and disordered interface formation

One of the most important questions surrounding interface structure in multilayers is the precise manner in which the interface structure evolves. In some systems it is observed that long-range crystalline order suddenly disappears as the bilayer period is reduced. In Mo/Ni, for instance, long-range structural coherence exists for all bilayer periods above about 15 Å, while samples with smaller bilayer periods, although still compositionally modulated, have a completely disordered structure [13, 14]. In other systems (*e.g.* Ni/Ti) the interfaces are disordered at all bilayer periods, but the number of atomic planes involved in the disordered phase takes a dramatic jump as the bilayer period is reduced below some critical value [2].

A key question, therefore, is exactly how this disordering occurs. The observation that the lattice parameter of the materials increases as the bilayer period decreases has lead Schuller [15] to suggest that this strain destabilizes the crystalline phase. A second explanation deals with the structure of a very thin film nucleating on a structurally dissimilar substrate. If the structural mismatch is small, the adsorbate will take on the lattice structure of the substrate. As the film grows thicker, at some point it will be energetically favorable for the film to relax to its own equilibrium bulk structure. If the structural mismatch between the film and substrate is large, however, the adsorbate cannot adopt the structure of the substrate, even for very thin layers. It may then be energetically favorable for a disordered or amorphous phase to form at the interface, if the interfacial energy of the substrate–amorphous layer interface is lower than that of a substrate–crystalline layer interface. This will certainly be true if an intermixed disordered phase forms at the interface. This disordered phase will be preferred up to a critical thickness, above which the layer will crystallize.

There is, therefore, an important link between the phenomenon of solid-state amorphization and the formation of interfaces in multilayers. As mentioned above, binary systems which exhibit SSAR tend to have a large size mismatch between the two components. We would therefore expect a multilayer of such a system to have disordered interfaces, and no long-range crystalline order for sufficiently small bilayer periods. This is indeed the case, as has been observed for many different systems.

What has not been clear, however, is the precise manner in which these interfaces form. Is one or both components crystalline as deposited, and then rendered amorphous by the subsequent deposition of the second component, or is there perhaps an asymmetry in the reaction, so that deposition of one component will amorphize the other, but not *vice versa*? It is also possible that neither is the case, *i.e.* that there is no significant intermixing during growth, but that the disordered interfaces form, by the solid-state amorphization reaction, subsequent to the deposition. These kinds of questions can only be answered directly by *in*

situ observations of the structure as it evolves during deposition.

3. Direct observation of amorphous interface formation

3.1. In situ *X-ray diffraction technique*

The development of structure in the near-surface region (0–100 Å below the surface) is in general difficult to observe because very few atoms are involved. In evaporation deposition, a variety of electron diffraction techniques are routinely employed *in situ*. These techniques cannot be applied to sputter deposition, because the high ambient gas pressure (typically 1–100 mTorr) causes the electrons to be strongly scattered. Grazing incidence X-ray scattering (GIXS), however, is a surface-sensitive structural tool which is ideal for *in situ* investigations, even in processes with high-process gas pressures. X-rays are not scattered by the gas ambient, the depth sensitivity is controllable, and precise quantitative structural measurements can be made, even in structurally disordered materials [16].

In the GIXS geometry (shown in Fig. 1), the X-rays are incident on the surface at a very small incident angle α, typically less than 1°. The X-rays are diffracted through the angle 2θ and exit the sample at the exit angle β, which is also very small. The scattering vector $\vec{q}$ then lies nearly in the plane of the sample. The d-spacings measured by GIXS are therefore also nearly in the plane of the sample. This is in contrast to traditional Bragg–Brentano diffraction geometry, which measures d-spacings which are parallel to the sample normal.

The surface sensitivity of GIXS arises from the limited penetration depth of X-rays incident on a solid material at a very small angle. If the angle of incidence is small enough, the X-rays can undergo total external reflection from the material, owing to the difference in index of refraction between the atmosphere and the solid material. Under total external reflection conditions the penetration depth of the X-rays is very limited, often less than 30 Å. In addition, because the X-rays undergo a phase shift of π upon reflection, constructive interference occurs and the electric field intensity (and thus X-ray intensity) are maximized near the surface at the critical angle. Therefore, a high degree of surface sensitivity can be achieved using the GIXS technique at incident angles near the critical angle for the material under observation. It should be noted that the critical angle is solely a function of the electron density of the material, and is therefore independent of the atomic structure at the surface.

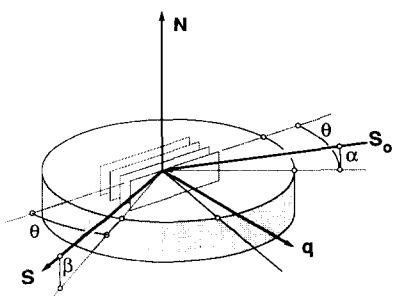

Fig. 1. Grazing incidence X-ray scattering geometry. It should be noted that the d-spacings measured by GIXS are in the plane of the sample.

3.2. *UHV deposition system with* in situ *GIXS capability*

Observations of the kind reported here require combining the functions of an ultra high vacuum (UHV) sputter deposition system with a z-axis goniometer. Such a system has been constructed by our research group, the details of which are reported elsewhere [17]. Briefly, the system consists of a UHV deposition chamber (capable of base pressure below 5×10^{-10} mTorr) with three independently shielded and shuttered d.c. magnetron sputter sources (see Fig. 2). Four samples sit on a carousel which allows each sample to be rotated in turn into the deposition/GIXS position. When the sample is moved into the deposition/GIXS position, it is aligned precisely with the goniometer axis via a gimble

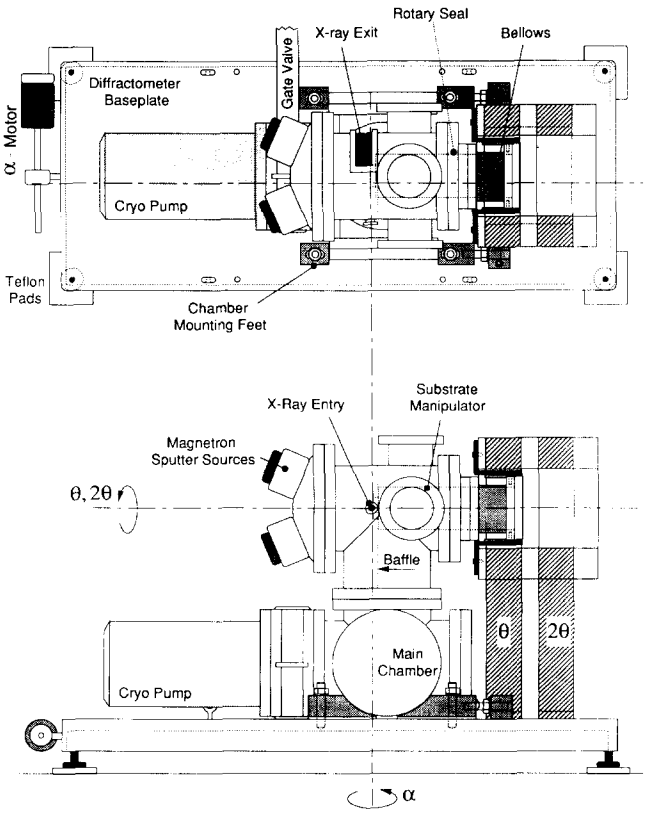

Fig. 2. UHV sputter deposition system with *in situ* GIXS capability.

mount through two micrometer-driven feedthroughs. This precise (within 1 mrad) alignment of the sample normal with the goniometer axis is essential to ensure that the incident angle (which controls the sampling depth) does not change with the θ rotation. The sample, along with the entire carousel, rotates with the θ axis of the goniometer.

The synchrotron X-ray beam enters the chamber through a 0.625 in diameter beryllium window. The diffracted beam exits the chamber through a 130° beryllium window which is welded directly onto the chamber. The entry and exit windows are protected from the sputter flux during deposition by extremely thin aluminium shields. The incident angle α is varied by rotating the entire chamber and goniometer together about a vertical axis which intersects the θ axis at the sample surface. This allows a precision in α of $\leqslant 0.1°$.

3.3. *Observation of amorphization reaction in Gd/Co system*

Our decision to study multilayers of Gd/Co was based on current interest in rare earth/transition metal alloys as magneto-optic materials, as well as our expectation that this system would exhibit a solid-state amorphization reaction. We initially fabricated Gd/Co multilayers with bilayer periods ranging from 10 Å to 500 Å. Symmetric X-ray diffraction and cross-section transmission electron microscopy revealed that, although these samples showed strong compositional modulation, they were entirely amorphous for all bilayer periods less than approximately 200 Å. For some samples, electron micrographs revealed that the last layer of Gd deposited on the multilayer was crystalline. We therefore postulated that for all except the smallest bilayer periods the Gd as deposited was crystalline, and rendered amorphous by reaction with subsequently deposited Co. To verify this hypothesis, and further explore the interface formation in the Gd/Co system, we undertook *in situ* observations of the amorphization reaction. These experiments, summarized here, are discussed at greater length elsewhere [18].

GIXS experiments were performed using 7100 eV X-rays on beam line 4-2 of the Stanford Synchrotron Radiation Laboratory (SSRL) in the UHV deposition chamber described earlier. The substrates were Si (100) wafers, and the sputtering was conducted in an argon atmosphere of 1.7×10^{-3} Torr. The base pressure of the chamber during these experiments was 4×10^{-9} Torr. The substrates were at ambient temperature during deposition; however, because the substrates are not cooled during deposition some slight increase in temperature is inevitable. The incident angles used for this study were near the critical angle for total external reflection (0.45° and 0.38° for Co and Gd respectively).

We first deposited a 135 Å thick Gd film onto a bare Si substrate. The diffraction pattern from this film, shown in Fig. 3, clearly shows the Gd (100) and Gd (002) HCP crystalline peaks. We then deposited 22 Å of Co onto the Gd film. After the Co deposition, the crystalline Gd peaks have disappeared and have been replaced by a broad diffraction feature characteristic of an amorphous phase. The observed decrease in intensity of the Gd peaks is much larger than can be accounted for by simple absorption of the X-rays by a Co layer on top of the Gd. Furthermore, the increase in intensity at angles above 36° (2θ) indicates that a qualitative change of the Gd structure has occurred. We saw no evidence for the existence of crystalline Co on top of the Gd, or for Gd–Co intermetallic phases in diffraction scans over wider angular ranges. We conclude from these observations that our original hypothesis was correct; upon deposition the Co diffuses immediately into the (previously deposited) crystalline Gd, forming an amorphous Gd–Co alloy by solid-state reaction. Similar experiments on other samples indicate that the Gd (100) and (002) peaks decay at approximately the same rate, leading us to conclude that either there is no asymmetry for diffusion of Co into Gd, or that this is not the limiting step for this reaction.

To confirm our conclusion that rapid diffusion of Co into the crystalline Gd causes the amorphization of the Gd, we conducted a second experiment in which we observed the intensity of the Co (002) peak as a function of the amount of Co deposited onto Gd. Co was

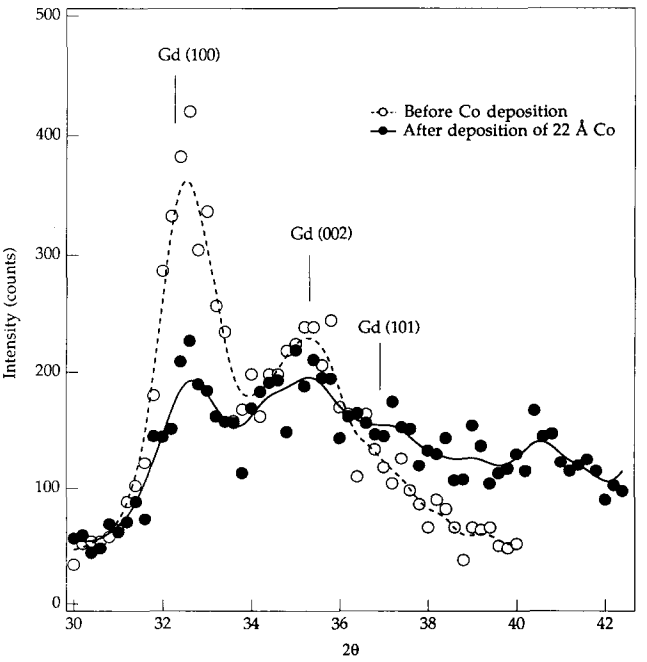

Fig. 3. GIXS pattern from a Gd film before and after Co deposition. The dramatic change in intensity of the Gd peaks should be noted. Positions of bulk Gd reflections are indicated.

deposited in 18 Å increments onto a 1350 Å thick crystalline Gd film. As shown in Fig. 4, no crystalline Co peaks are observed for thicknesses of Co less than 63 Å. At 63 Å, however, a strong Co (002) peak suddenly appears. It should be noted that this peak is significantly stronger than the weakest peak which could be distinguished from the background. After several observations of the Co (002) reflection between Co depositions, we undertook to record the intensity of this peak in real time during deposition. We combined these data with the known Co deposition rate to obtain the intensity of the Co (002) peak as a function of Co thickness. (The peak did not shift during the real time observation.) The intensity of the Co (002) peak, as determined from the combined incremental and real time data, is shown in Fig. 5.

Two explanations for the evolution of the Co (002) peak intensity are possible. First, one could conclude that any Co deposited on a crystalline Gd surface diffuses immediately into the Gd, resulting in the formation of an amorphous Gd–Co alloy. A second explanation would be to postulate the existence of a disordered Co-rich phase on the Gd surface which does not become crystalline until a certain critical thickness is attained. If this second case were true, we would expect that the large increase in the Co (002) peak intensity (when a relatively thick surface layer of Co crystallizes) would be followed by much smaller increases in intensity. However, as shown in Fig. 4, subsequent Co deposition results in continued large increases in intensity. This is consistent with the first explanation.

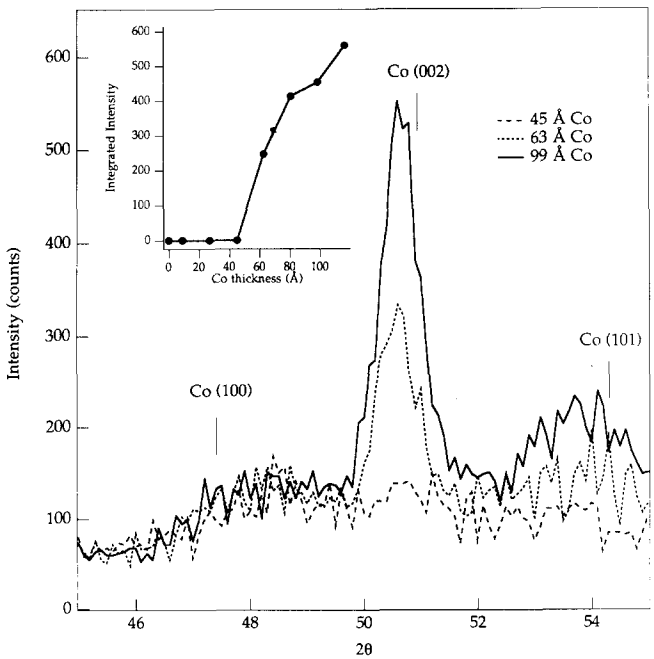

Fig. 4. Observation of Co peaks during Co deposition onto a Gd film.

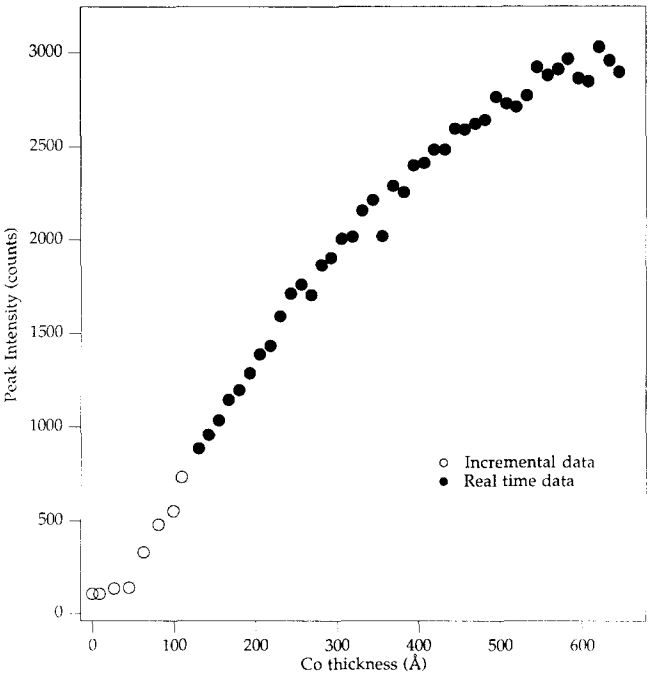

Fig. 5. Evolution of the intensity of the Co (002) peak as a function of Co thickness deposited.

We conclude, therefore, that the first stage of the reaction is the diffusion of Co into Gd and the resulting amorphization reaction. Nucleation and growth of crystalline Co occurs later, after the amorphization reaction is essentially complete.

4. Discussion

4.1. Kinetic model

One remarkable aspect of amorphous interface phase formation during growth is the long diffusion distances occurring during the relatively short deposition times. Simple application of the expression $x \approx \sqrt{Dt}$ shows that diffusion distances in the order of 100 Å during typical deposition times require the diffusivity to be about 10^{-14} cm^2 s^{-1}. If the atomic mobility after growth were the same as during growth, a 1000 Å bilayer period sample would amorphize over the course of about 3 h. However, we observe no changes in composition profile and degree of crystallinity after storage of periods as long as several months. Clearly there are differences in the kinetics during and after growth.

In order to understand further the formation of the amorphous phase regions during deposition, a simple kinetic model was developed. This model is based on a simple layer growth model for the amorphous layer. Figure 6 shows the free energy of the HCP Co, HCP Gd and the amorphous phase as a function of Co atomic fraction, n_{Co}, calculated by the method of Miedema [19, 20]. Shown on this figure are the common

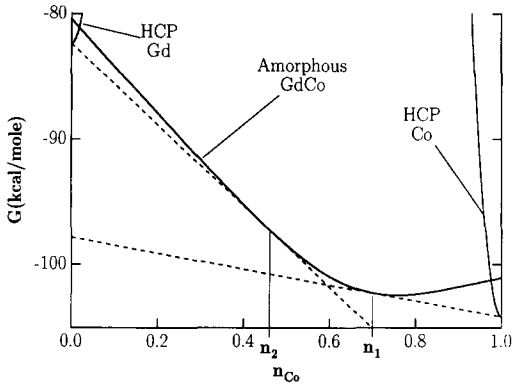

Fig. 6. Free energy as a function of the atomic fraction of Co for the amorphous phase, found from the Miedema method. The free energies for pure HCP Co and Gd are found from standard thermodynamic tables, and the free energy *vs.* composition for these phases is schematically represented as a steeply rising parabola, since there is very limited solid solubility in either phase. The equilibrium concentrations, n_1 and n_2, are found by the common tangent construction.

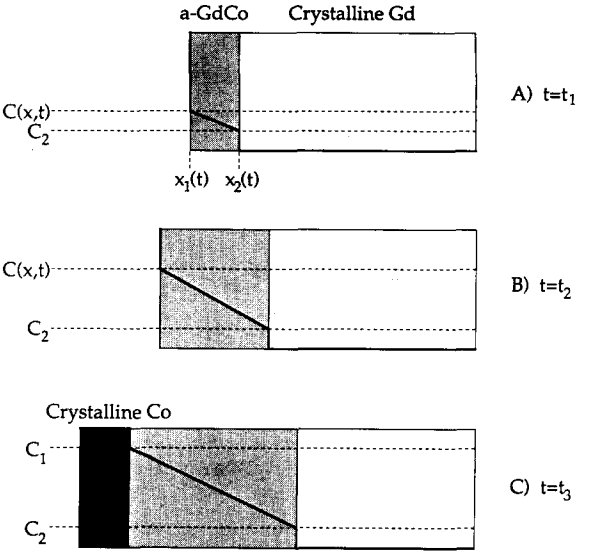

Fig. 7. Schematic representation of the reaction sequence for amorphous phase formation during growth.

tangent points which determine the equilibrium atomic fractions, n_1 and n_2, of Co in amorphous GdCo (a) in contact with the terminal HCP phases. Co deposited onto a Gd surface reacts to form an amorphous surface layer with an atomic fraction near n_2 at the a–Gd interface. Further deposition of Co onto the surface will diffuse into the amorphous phase and cause the surface Co concentration to rise and the width, x_2-x_1, of the amorphous layer to increase. When the surface concentration reaches c_1, further deposition of Co will result in growth of HCP Co on the surface. According to our experimental results, this will occur when the total amount of Co deposited corresponds to about 50 Å of HCP Co. These steps are shown schematically in Fig. 7.

The diffusion equation to be solved can be formulated as follows:

$$\frac{\partial c(x,t)}{\partial t} = \frac{\partial}{\partial x} D(c(x,t)) \frac{\partial c(x,t)}{\partial x}$$

$$c(x_2(t)) = c_2$$

$$J_s = D(c(x,t)) \left.\frac{\partial c(x,t)}{\partial x}\right|_{x=x_1} - c(x_1,t) \frac{dx_1(t)}{dt} \tag{1}$$

$$c_2 \frac{dx_2(t)}{dt} = D(c,(x,t)) \left.\frac{\partial c(x,t)}{\partial x}\right|_{x=x_2} \tag{2}$$

$$x_1(0) = 0$$

$$x_2(0) = 0$$

where $c(x,t)$ is the concentration of Co in the amorphous phase, J_s is the flux of Co atoms from the vapor phase, $D(c)$ is the composition-dependent diffusivity, and $x_1(t)$ and $x_2(t)$ are the interface positions, as shown in Fig. 7. The diffusivity, $D(c)$, is dominated by the rapidly moving species (Co), hence:

$$D(c) = n_{Co} D_{Gd} + n_{Gd} D_{Co}$$

$$\approx n_{Gd} D_{Co}$$

where D_{Co} and D_{Gd} are the intrinsic diffusivities given by the tracer or self-diffusivities times the thermal factor, and n_{Co} and n_{Gd} are the number fractions of their respective species. In the case where atomic volumes of each species are environment independent, we can find:

$$n_{Gd}(x,t) = \frac{1-\Omega_{Co} c(x,t)}{1-(\Omega_{Co}-\Omega_{Gd}) c(x,t)} \tag{3}$$

where Ω_i is the atomic volume of the ith atomic species.

The problem as formulated above is not amenable to analytical solution, and must be approached by numerical methods for partial differential equation solving. However, by making a few simplifying assumptions we can gain some understanding of the phenomenon at hand. We first examine the solution to the diffusion equation in semi-infinite media with concentration-independent diffusivity, zero initial concentration, and a constant flux at the surface. This can be solved analytically using the method of Laplace transforms to give a concentration with a nearly linear depth dependence, and a surface concentration given by:

$$c'(0,t) = 2J_s \sqrt{\frac{t}{D\pi}} \tag{4}$$

Assuming this form for the concentration at $x=x_1(t)$, a linear concentration profile and a concentration in-

dependent diffusivity, eqns. (1) and (2) lead to:

$$J_0 = \frac{Dc_2}{w(t)} - \frac{4J_s^2 t}{c_0 \pi w(t)} + 2J_0\sqrt{\frac{t}{\pi D}}\frac{\mathrm{d}w(t)}{\mathrm{d}t} \quad (5)$$

which is just an ordinary differential equation in $w(t) = x_2(t) - x_1(t)$, which is the width of the amorphous layer as a function of time. This can be solved numerically using relatively simple numerical routines, for example *Mathematic Version 2.0.*

We can obtain an estimate of the diffusivity from this simple model. We take the equilibrium volume fractions from the common tangent construction of Fig. 6 ($n_{Co1} = 0.70$ and $n_{Co2} = 0.46$) and convert them to the equilibrium concentrations by inverting eqn. (3). Equation (4) then predicts that for typical deposition rates of ≈ 2 Å s^{-1} the diffusivity must be about 5×10^{-14} cm^2/s (in remarkable agreement with the estimate obtained from diffusion distance considerations). The solution of eqn. (5) for this case shows an amorphous phase width of about 100 Å, in agreement with the observed behavior of multilayer samples.

Large bilayer period ($\geqslant 250$ Å) Gd/Co multilayers produced in our laboratory show thin layers of crystalline Gd and Co between extensive amorphous Gd–Co alloy interfaces. Given the large bulk interdiffusivity predicted by the model above (based on the speed of the reaction during deposition), one must ask what prevents the amorphization from going to completion in multilayer samples. There is no obvious reason why the reaction should terminate, and so it seems likely that there are kinetic processes occurring during deposition, allowing the reaction to proceed, which are not available after deposition is complete.

One clear difference between during- and after-growth kinetics is that after growth the source of Co is a HCP Co layer, while during growth the Co arrives as energetic single atoms, which can be expected to have greater reactivity and mobility. In addition, the availability of a free surface during growth may allow rapid lateral diffusion of Co to fast diffusion paths into the Gd (*e.g.* Gd grain boundaries). Furthermore, transport of Co from the HCP phase into the amorphous phase will be accompanied by a reverse flux of vacancies due to the large asymmetry of the diffusion process ($D_{Co} \gg D_{Gd}$). Vacancy diffusion through the HCP Co will not be as rapid as diffusion of Co in Gd, and might be expected to occur at a much lower rate, more typical of the self-diffusivity of Co. This vacancy diffusion might therefore be the rate-limiting step for the amorphization reaction from the crystalline Co phase. During growth, however, the free surface is a sink for vacancies and this kinetic limitation is eliminated.

5. Conclusions

There is a fundamental link between the phenomenon of solid-state amorphization and the formation of disordered interfaces during vapor phase deposition of thin film multilayers. The development of long-range crystalline order in multilayers is inhibited by the formation of disordered interfaces, which are caused by an amorphization reaction resulting from intermixing at the interfaces during deposition. We have observed that the formation of disordered interfaces in the Gd/Co system is due to rapid diffusion of Co into Gd, resulting in amorphization of the originally crystalline Gd. A simple model allows an estimate of the interdiffusion coefficient, leading to the conclusion that there are significant kinetic differences between processes occurring during growth and those that occur afterward.

References

1 R. B. Schwarz and W. L. Johnson, *Phys. Rev. Lett., 51*(5) (1983) 415.
2 B. M. Clemens and R. Sinclair, *MRS Bulletin, XV*(2) (1990) 19–38.
3 W. L. Johnson, *Program. Mater. Sci., 30* (1986) 81–134.
4 B. M. Clemens, W. L. Johnson and R. B. Schwarz, *J. Non-Cryst. Solids, 61&62* (1984) 817.
5 M. A. Hollanders, B. J. Thijsse and E. J. Mittmeijer, *Phys. Rev. B, 42* (1990) 5481–5494.
6 H. Bakker, *J. Less-Common Met., 105* (1983) 129.
7 Z. S. Shan, S. Nafis, K. D. Aylesworth and J. D. Sellmyer, *J. Appl. Phys., 63* (1988) 3218–3220.
8 C. F. Majkrzak, D. Gibbs, P. Böni, A. I. Goldman, J. Kwo, M. Hong, T. C. Hsieh, R. M. Fleming, D. B. McWhan, Y. Yafet, J. W. Cable, J. Bohr, H. Grimm and C. L. Chien, *J. Appl. Phys., 63* (1988) 3447–3452.
9 A. Maeda, T. Satake, T. Fujimori, H. Tajima, M. Kobayashi and K. Kuroda, *J. Appl. Phys., 65* (1989) 3845–3848.
10 M. Matsuura, R. Petkie, G. Singco and K. N. Tu, *Mater. Sci. Eng., A133* (1991) 551–554.
11 D. J. Webb, R. G. Walmsley, K. Parvin, P. H. Dickinson, T. H. Geballe and R. M. White, *Phys. Rev. B, 32* (1982) 4667–4675.
12 B. M. Clemens and J. G. Gay, *Phys. Rev. B, 35* (1987) 9337.
13 B. M. Clemens, *J. Less-Common Met., 140* (1988) 57–66.
14 M. R. Khan, C. S. L. Chun, G. P. Felcher, M. Grimsditch, A. Kueny, C. M. Falco and I. K. Schuller, *Phys. Rev. B, 27* (1983) 7186.
15 I. K. Schuller and A. Rahman, *Phys. Rev. Lett., 50*(18) (1983) 1377.
16 P. H. Fuoss and S. Brennan, *Annu. Rev. Mater. Sci., 20* (1990) 365.
17 A. P. Payne, B. M. Clemens and S. M. Brennan, *Rev. Sci. Instrum., 63*(1) (1992) 1147.
18 T. C. Hufnagel, S. Brennan, A. P. Payne and B. M. Clemens, *J. Mater. Sci., 7*(8) (1992) 1976.
19 A. R. Miedema, *Philips Tech. Rev., 36* (1976) 217.
20 B. M. Clemens, *Phys. Rev. B, 33*(11) (1986) 7615.